NUCL SCI TECH (2022) 33:130
https://doi.org/10.1007/s41365-022-01112-z

Beam–beam effects and mitigation in a future proton–proton collider

Li-Jiao Wang[1,2,3] · Tanaji Sen[4] · Jing-Yu Tang[1,2,3] · Lin-Hao Zhang[1,2,3]

Received: 16 June 2022 / Revised: 2 September 2022 / Accepted: 3 September 2022 / Published online: 11 October 2022

Abstract The beam–beam effects in a hadron collider with an unprecedented energy scale were studied. These effects are strongly related to the attainable luminosity of the collider. Long-range interactions were identified as the major factor limiting the dynamic aperture, which is strongly dependent on the crossing angle, $\beta *$, and bunch population. Different mitigation methods of the beam–beam effects were addressed, with a focus on the compensation of long-range interactions by electric current wires. The CEPC-SPPC project is a two-stage large circular collider, with a first-stage circular electron–positron collider (CEPC) and a second-stage super proton–proton collider (SPPC). The design of the SPPC aims to achieve a center-of-mass energy of 75 TeV and peak luminosity of approximately 1×10^{35} cm^{-2} s^{-1}. We studied the beam–beam effects in the SPPC and tested the effectiveness of the mitigation methods. We found that with compensation using electric current wires, the dynamic aperture is at an acceptable level. Moreover, considering the significant emittance damping in this future proton–proton collider, the beam–beam effects and compensation are more complicated and are studied using long-term tracking. It was found that with a smaller emittance, the head-on interactions with a crossing angle become more prominent in reducing the beam stability, and combined head-on and long-range compensation is needed to improve the beam quality. When the reduction in population owing to burn-off was included, it was found that the coupling between the transverse and longitudinal planes at smaller emittance is the main driving source of the instabilities. Thus, crab cavities and emittance control are also necessary than just the compensation of the long-range interactions to improve the beam stability. This study serves as an example for studying the beam–beam effects in future proton–proton colliders.

Keywords Particle collider · Beam-beam effects · Luminosity · Tune footprint · Dynamic aperture

This work was supported by the National Natural Science Foundation of China (Nos. 11575214, 11527811, and 11805218) and the Fermi Research Alliance, LLC, under contract no. DE-AC02-07CH11359 with the U.S. Department of Energy.

✉ Jing-Yu Tang
tangjy@ihep.ac.cn

1 Institute of High Energy Physics, CAS, Yuquan Road 19B, Beijing 100049, China

2 University of Chinese Academy of Sciences, CAS, 19A Yuquan Road, Beijing 100049, China

3 Spallation Neutron Source Science Center, Dongguan 523803, China

4 Fermi National Accelerator Laboratory, P.O. Box 500, Batavia, IL 60510, USA

1 Introduction

Beam–beam (B–B) interactions, including head-on interactions (HOIs) and long-range interactions (LRIs), are key issues in high-intensity colliders [1–4]. Future proton–proton colliders will require high luminosity; thus, the B–B interactions will be pushed to the limit, most probably exceeding the limits in the current large hadron collider (LHC) or its upgrade the high-luminosity large hadron collider (HL-LHC). As the highest energy collider in the world, the LHC plays a leading role in the frontiers of particle and heavy-ion physics. For the latter, for example, some new studies on the collective flows of quark matter have been performed [5–7]. Based on the parameters of the super proton–proton collider (SPPC), the second stage of a Chinese proposal for the future super-scale collider, the B–B effects, and mitigation methods must be studied. In general, B–B interactions can be mitigated by adjusting the beam parameters or compensating the B–B interactions.

The SPPC is planned as an energy frontier collider and discovery machine beyond the LHC [8]. The circular electron–positron collider (CEPC) and SPPC will be constructed in the same tunnel, 100 km in circumference. Figure 1 shows the layout of the SPPC [9]. The double-ring collider consists of two long straight sections (LSS) of length 4300 m, six straight sections of length 1250 m, and eight arc areas. LSS3 and LSS7 are used for high-luminosity proton–proton collisions. In the CEPC, LSS1 and LSS5 are electron–positron collision areas. In the SPPC, the two beams are independently accelerated in their own beam pipes in two opposite directions. They are transported to the interaction region (IR) with a length of 310 m and collided at a crossing angle at each interaction point (IP). Table 1 summarizes the main parameters of the SPPC [8–9]. The emittance damping in both the transverse and longitudinal phase planes is significant. Considering that the emittance shrinkage changes the behavior of B–B interactions, the effects and validity of compensation with shrinking emittance also need to be studied, an issue that has not been carefully investigated before.

In this study, the B–B effects and their mitigation in the SPPC were studied in the weak–strong approximation using the BBSIM code [10]. The weak beam denotes that the sampling beam is affected by the B–B interactions and compensation, and the strong beam denotes the perturbation source of the B–B interactions, which remain unaffected by these interactions. Section 2 presents the theoretical aspects of the luminosity and B–B interactions. The simulation results and analysis are presented in two parts: the first part, in Sect. 3, considers constant emittance in both planes by assuming an emittance heating mechanism; the second part, in Sect. 4, considers the transverse emittance shrinking and particle burn-off. The main conclusions are summarized in Sect. 5.

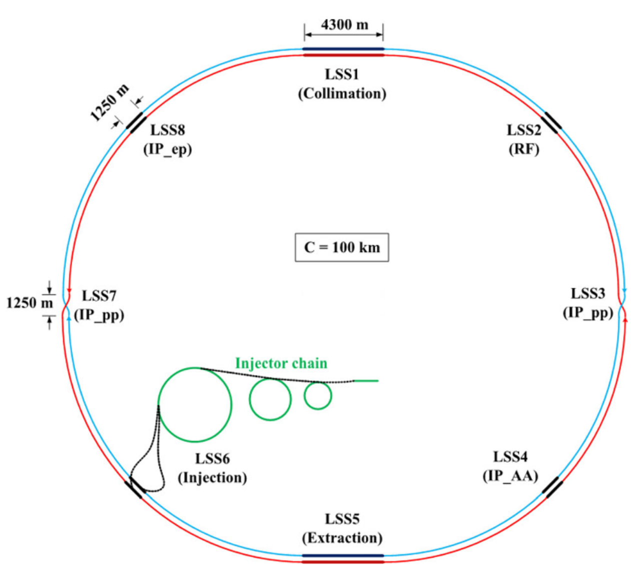

Fig. 1 (Color online) Layout of the super proton–proton collider (SPPC). There are two main interaction points (IPs) (IP_pp) and two reserved IPs (IP-ep and IP-AA)

Table 1 SPPC main parameters

Parameter	Value
Beam energy at collisions (TeV)	37.5
Number of IPs	2
Number of bunches	10,080
β^* (m)	0.75
Crossing angle (μrad)	110
Intensity (10^{11})	1.5
Norm. trans. emittance (μm)	2.4
Bunch spacing (ns)	25
Rms bunch length (mm)	75.5
Rms momentum spread (10^{-5})	7.07
Peak luminosity (10^{35} cm^{-2} s^{-1})	1.0
Reduction factor in luminosity	0.85
Beam–beam parameter of each IP	0.0075
Length of common area (m)	310
Number of long-range interactions (LRIs)	164
Separations at first LRI (σ)	12
Range of separations at LRI (σ)	9–19
Transverse emittance damping time (h)	2.35
Longitudinal emittance damping time (h)	1.175
Inelastic pp cross section (mbarn)	105
Total pp cross section (mbarn)	148

2 Relevant theory on luminosity and beam–beam effects

Luminosity is a major parameter for evaluating the beam performance of colliders and is limited by various factors. B–B interactions have long been known to limit luminosity in hadron colliders; in particular, LRI plays an important role [3, 11–14]. Three indicators, including the tune footprint, frequency map analyses (FMAs), and dynamic aperture (DA), are used to study the beam behaviors, and some mitigation methods are summarized.

2.1 Luminosity limitation from a crossing angle

The crossing angle at an IP is usually designed such that more bunches can be accumulated in the collider and higher luminosity can be attained. However, the crossing angle reduces the overlapping region between the two bunches during collision, and the luminosity in each collision decreases, as expressed in the following equation:

$$L = \frac{n_{\mathrm{b}} N_{\mathrm{b}}^2 f}{4\pi\sigma_x^*\sigma_y^*}\frac{1}{\sqrt{1+\left[(\phi\sigma_z)/(2\sigma_x^*)\right]^2}}. \tag{1}$$

The first term in Eq. (1) is the ideal luminosity, and the second factor is the luminosity reduction owing to the crossing angle. The asterisk indicates the IP value. σ_x* and σ_y* are the RMS horizontal and vertical beam sizes, respectively. L, N_{b}, n_{b}, f, ϕ, and σ_z are the luminosity, bunch population, number of bunches, revolution frequency, crossing angle, and RMS longitudinal beam size, respectively.

The crossing angle at the IP is created using a set of dipoles [15–16]. After adding the crossing angle, the beam orbit is displaced in the IR quadrupoles, leading to unwanted anomalous dispersion at the IP [15, 17]. This can increase the beam size as follows:

$$(\sigma_{x,y}^*)^2 = \varepsilon_{x,y}\beta_{x,y}^* + (\sigma_{\mathrm{p}} D_{x,y}^*)^2, \tag{2}$$

where $\varepsilon_{x,y}$, $\beta_{x,y}$, and $D_{x,y}$ are the horizontal and vertical emittance, beta function, and dispersion, respectively, and σ_{p} is the RMS momentum spread. Equation (1) shows that the ideal luminosity decreases, and the reduction factor due to the crossing angle increases with a larger horizontal beam size. The derivative of luminosity with respect to σ_x is

$$\frac{\mathrm{d}L}{\mathrm{d}\sigma_x^*} = -2fn_{\mathrm{b}}N_{\mathrm{b}}^2 \Big/ \left(\pi\sigma_y^*\left(4(\sigma_x^*)^2+\sigma_z^2\phi^2\right)\sqrt{4+\frac{\sigma_z^2\phi^2}{(\sigma_x^*)^2}}\right), \tag{3}$$

which shows that the luminosity monotonously decreases with increasing σ_x. In addition, the luminosity is restricted by the synchro-betatron coupling caused by the finite dispersion at the IP [18].

The scheme proposed in Ref. [15] provides a method for correcting anomalous dispersion in both planes. Two pairs of quadrupole correctors are placed in the neighboring arc region (where there was a horizontal dispersion) on both sides of each IR. In each pair, the two quadrupoles are separated by an π in phase advance and have the same strengths and opposite polarities to cancel the changes in the beta function from each quadrupole corrector. For an IR with vertical crossing, a pair of skew quadrupoles is used because these quadrupoles transform the horizontal dispersion into the vertical plane.

The dispersion correction scheme limits the achievable ranges of crossing angle and β*, while maintaining the required level of correction. Moreover, the ranges of β* and crossing angle are determined by the available physical aperture. The minimum aperture occurs in the inner triplet at the location of the maximum β and decreases linearly with increasing crossing angle. Equation (1) shows that the luminosity strongly depends on the transverse beam size and crossing angle. Thus, the targeted level of dispersion correction and the physical aperture limit the attainable luminosity.

2.2 Beam behaviors related to the beam–beam interactions

The B–B interactions are nonlinear kicks, so that the particles oscillating with different amplitudes have different tune shifts. The tune distribution of all the particles in the frequency space is called the tune footprint. The theoretical formula to calculate the tune shift in the horizontal plane for particles with different amplitudes is [4]

$$\Delta v_x(a_x,a_y,d_x,d_y,r) = \frac{4\pi C}{\varepsilon_x} \int_0^1 \frac{e^{-(p_x+p_y)}}{\upsilon[\upsilon(r^2-1)+1]^{1/2}}\sum_x\sum_y \mathrm{d}\upsilon, \tag{4}$$

where

$$\sum_x = \sum_{k=0}^{\infty}\frac{\left(\frac{a_x}{d_x}\right)^k}{k!}\Gamma\left(k+\frac{1}{2}\right)\left[I_k(s_x)\left(\frac{2k}{a_x^2}-\upsilon\right)+I_{k+1}(s_x)\frac{s_x}{a_x^2}\right], \tag{5}$$

$$\sum_y = \sum_{l=0}^{\infty}\frac{\left(\frac{a_y}{d_y}\right)^l}{l!}\Gamma\left(l+\frac{1}{2}\right)I_l(s_y), \tag{6}$$

$$C = \frac{N_{\mathrm{b}} r_{\mathrm{p}}}{(2\pi)^3\gamma_{\mathrm{p}}},\ r = \frac{\sigma_y}{\sigma_x},\ p_x = \frac{\upsilon}{2}\left(a_x^2+d_x^2\right),\ p_y = f\frac{\upsilon}{2}\left(a_y^2+d_y^2\right),$$

$$s_x = \upsilon a_x d_x,\ s_y = f\upsilon a_y d_y,\ f = r^2/\left(\upsilon(r^2-1)+1\right),$$

where υ is the integration variable in Eq. (4); a_x and a_y are the particle amplitudes normalized by the beam transverse size; d_x and d_y are the separations normalized by the beam transverse size; r is the aspect ratio; r_{p} is the classical proton radius; and γ_{p} is the relativistic Lorentz factor. $I_n(s_n)$ is the modified Bessel function of the first kind and $\Gamma(n+0.5)$ is the gamma function. A similar equation exists for Δv_y; more details can be found in Ref. [4]. These expressions show that the tune shifts depend on the normalized separations, amplitudes, and aspect ratio of the strong beam, in addition to the brightness parameter N_b / ($\gamma_p \varepsilon_x$).

The B–B parameter is the largest tune shift owing to the HOIs in a bunch. For these interactions without a crossing angle, it is expressed as

$$\xi_{x,y} = \frac{r_p N_b \beta^*_{x,y}}{2\pi\gamma_p \sigma_{x,y}(\sigma_x + \sigma_y)}, \quad (7)$$

where $\xi_{x,y}$ denote the B–B parameter in the horizontal or vertical plane. In the presence of a crossing angle in the horizontal plane, it is modified as [19]

$$R = \frac{1}{\sqrt{1 + \left[(\phi\sigma_z)/(2\sigma^*_x)\right]^2}}, \quad (8)$$

$$\xi_x = \frac{r_p N_b \beta^*_x R^2}{2\pi\gamma_p \sigma_x(\sigma_x + R\sigma_y)}, \quad (9)$$

$$\xi_y = \frac{r_p N_b \beta^*_y R}{2\pi\gamma_p \sigma_y(\sigma_x + R\sigma_y)}. \quad (10)$$

The B–B parameter is different in both the transverse planes, even for round beams, and it decreases with an increasing crossing angle.

FMA has been widely used as an early indicator of particle instability by calculating the diffusion of tunes. The diffusion parameter is defined as follows [20]:

$$D = \log_{10}\left[\sqrt{(\nu_{x2} - \nu_{x1})^2 + (\nu_{y2} - \nu_{y1})^2}\right], \quad (11)$$

where $\nu_{x1,y1}$ and $\nu_{x2,y2}$ are tunes from the first and second halves of the tracking turns using a fast Fourier transform (FFT), respectively. A larger tune diffusion suggests stronger destructive effects of the nonlinearity.

The dynamic aperture is defined as the maximum stable transverse amplitude, which typically requires numerical tracking. We choose the initial transverse distribution to be a 2D Gaussian in the (x, y) space as $x = N\sigma_x\cos\theta$, $y = N\sigma_y\sin\theta$, $x' = y' = 0$, and θ ranges from 0 to π/2 in steps of 15°. N is a real parameter whose range varies with the problem under study.

Resonance excitation due to the B–B interactions was the main mechanism affecting the single-particle stability in our study. The HOI excited even resonances, and the LRI activated resonances of any order. In the case of the crossing scheme, the crossing angle can drive additional odd resonances. If the resonances overlap, the particles may be trapped and move outward to the aperture limit defined by the collimation system [21]. Meanwhile, the crossing scheme couples the transverse plane to the longitudinal plane, which activates synchro-betatron resonances, another mechanism that deteriorates beam stability.

2.3 Mitigation of long-range interactions with modified beta star and crossing angle

The LRI kick strongly depends on the transverse separation normalized by the RMS transverse size of the strong beam. The transverse separation can be controlled in two ways. One is to increase the crossing angle, which changes the absolute transverse separation; the other is to increase β^*, which changes the beam size.

Increasing the crossing angle has many negative effects, such as lower luminosity, enhanced synchro-betatron resonances, lower relative physical aperture, and worse nonlinearities for the inner quadrupole triplet. In this case, the countermeasure is to use crab cavities to recover the luminosity and minimize the synchro-betatron resonances, assuming their successful operation in the LHC. However, the smaller relative physical aperture and worse nonlinearities of the triplet remain important limitations.

Increasing β^* reduces β at LRIs, which can improve the beam stability, but causes lower luminosity. However, in future hadron colliders with significant synchrotron radiation, the emittance evolution follows an exponential decay:

$$\varepsilon(t) = \varepsilon(0)e^{-(t/\tau)}, \quad (12)$$

where τ is the transverse emittance damping time (= 2.35 h in the SPPC, see Table 1). The emittance shrinking can help increase the relative transverse separation at LRIs and thus mitigate their strength. This provides the possibility of squeezing β^* dynamically to recover luminosity while maintaining the impact of the LRIs under control. However, the emittance reduction will enhance the HOIs and possibly make them become dominant in the later stages of the luminosity run. Dedicated studies of B–B interactions need to be conducted together with the evolution of the beam parameters, which is discussed in Sect. 4.

2.4 Compensation of long-range interactions with current-carrying wires

The LRI compensation (LRC) with current-carrying wires was first proposed and studied in 2000 [22]. Each wire was placed parallel to the beam trajectory to compensate for the LRI acting on the beam. In general, the wire kick depends on (a) the wire current (I), (b) the wire length (L), (c) $\beta_{x,y}$ at the wire, (d) phase advances between the wire and LRI locations, and (e) the transverse distance from the beam to the wire. Parameters (a) and (b) can be determined by assuming the same integrated strength of the wire and the LRI, which can be expressed as [23]

$$IL_w = N_b n_{LR} ec, \quad (13)$$

where N_b is the bunch population; n_{LR} is the number of LRIs that need to be compensated; e is the elementary charge; and c is the speed of light.

Parameters (c), (d), and (e) need to be selected according to the distribution of the LRIs and lattice features with several requirements. First, the ratio β_x/β_y at the wire should match that at the LRI locations [24]. Second, it is preferable to place the wire after the first separation dipole to avoid affecting another beam. Third, the phase advances between the wire and the LRI locations should be an integer multiple of π to better compensate for the LRI kicks [24]. Finally, the transverse normalized separation at the wire must match that at the LRI location. It is impossible to meet all the requirements, and therefore, compromises are necessary in choosing the location of the wires for optimum compensation.

2.5 Compensation of head-on interactions with electron lens

HOI compensation (HOC) using electron beams was first proposed and studied in 1993 [25–26]. A low-energy electron beam is introduced to collide with a proton beam, which can compensate for the kick given to this beam delivered by the opposing beam. The device used to provide the electron beam is called an e-lens. Generally, the kinetic energy of electrons is approximately 5–10 keV. To compensate for the effect of HOIs, the following conditions, similar to those for long-range compensation, need to be met [27–28]:

(a) The electron beam should exhibit the same transverse distribution as the proton beam.

(b) The number of electrons (N_e) overlapping with a proton bunch, bunch population of protons (N_p), and relative speed of electrons (β_e) should satisfy

$$N_e(1 + \beta_e) = N_p. \tag{14}$$

Once β_e is selected, the number of electrons can be determined by the bunch population of protons.

(c) The electron beam size should be the same as that of the proton beam at the e-lens.

(d) The ratio of the lattice horizontal and vertical β functions at the e-lens should match the ratio at the IP.

(e) The phase advance between the HOI and e-lens should be an odd multiple of π to compensate for the tune shift and resonance driving terms.

It is also difficult to fulfill all the conditions in practice when compensating for the HOI.

3 Simulation results on the beam–beam effects with constant emittance

In this section, simulations are performed assuming that the emittance in the transverse and longitudinal phase planes is constant by applying external noise. This assumption is made to simplify the simulations described in this section, but will be neglected in Sect. 4.

The SPPC nominal IR lattice design is first presented and β^* is selected under different constraints. Next, the B–B effects were studied to determine which types of interactions are dominant. Finally, mitigation methods were examined to improve the beam stability.

3.1 Nominal IR lattice

The IR lattice is a typical left/right antisymmetric optics with the same β^* value in the two transverse planes. The free space from the IP to the first triplet quadrupole is 45 m. The inner triplet is responsible for producing a small β^* of 0.75 m, which causes a maximum β of 18,600 m in the triplet. The two separation dipoles separate the beams into their own pipes. The outer triplet matches the beta and dispersion to the dispersion suppressor. Figure 2 shows the beta functions in the IR with a horizontal crossing angle (IR3). The first-order chromaticity in the ring is corrected by sextupoles, but a second-order chromaticity correction system has not yet been designed and is not considered here.

In the SPPC, crossing is generated in the horizontal plane at IP3 and vertical plane at IP7 to compensate for the tune shifts from the LRIs. Four dipole correctors per beam in each IR are used to steer the closed orbit, and four

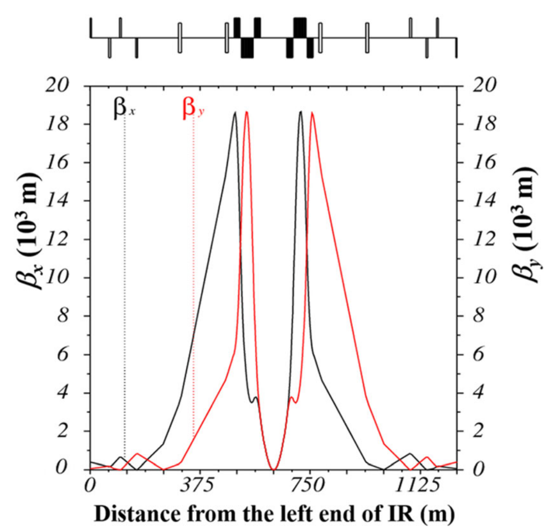

Fig. 2 (Color online) Beta functions in the interaction region (IR) with a horizontal crossing angle

quadrupole correctors are placed in each IR to correct the anomalous dispersion owing to the crossing angle. Figure 3 shows the layout of the dipole and quadrupole correctors for the two IRs. The phase advance of each orbit and quadrupole corrector from the IP is marked in the plot. In Table 2, the dispersions at both IPs and the maximum horizontal and vertical dispersions in IR3, IR7, and the entire ring are listed. Comparing the third and fourth columns, the anomalous dispersion is found to be well compensated by the quadrupole correctors. Figure 4 shows the corrected dispersion in the two IRs and their neighboring arc regions. With a corrected dispersion of 0.001 m at the IP, Eq. (2) shows that the luminosity loss with a momentum spread of approximately 0.004% (equal to the nominal RMS value) is negligible.

As mentioned in Sect. 2.1, the values of the crossing angle and β^* affect the validity of the dispersion correction scheme. Three β^* values and different initial parasitic separations were considered to study the dispersion correction scheme. The initial parasitic separation in the drift space before the triplet quadrupoles is normalized by the RMS beam size σ and can be approximated by the following formula for a small β^*

$$d = \phi s \Big/ \sqrt{\varepsilon(\beta^* + \frac{s^2}{\beta^*})} \approx \frac{\phi\sqrt{\beta^*}}{\sqrt{\varepsilon}}, \tag{15}$$

where s is the distance of the parasitic interaction location from the IP.

First, the initial separation was maintained constant at 12σ; β^* was varied; and the crossing angle scale was $1/\sqrt{\beta^*}$. Table 2 indicates that the maximum (horizontal, vertical) dispersions ($D_x^{\max}$, $D_y^{\max}$) are (2.8 m, 0 m), respectively, without a crossing angle. With the crossing angles, the quadrupole correctors can correct $D_x^{\max}$ to approximately 2.8 m when β^* is 0.5, 0.75, and 1.00 m. The dispersion at the IP was corrected to less than 0.005 m, decreasing the luminosity by less than 0.2%. Figure 4 shows that the correction of the vertical dispersion in IR7 is slightly worse than that of the horizontal dispersion in IR3. This occurs because the skew quadrupole correctors are not at the ideal locations, where the phase advances between the quadrupole correctors and the IP should be half-integer multiples of π, but the errors are still within the acceptable level.

Next, we increased the initial separation from 12σ to 20σ for the same three values of β^* indicated above. Similarly, the horizontal dispersion was well corrected in each case, but the vertical dispersion, D_y, was not. Figure 5 shows the maximum vertical dispersion, $D_y^{\max}$, with and without the quadrupole correctors. In the entire range of separations, $D_y^{\max}$ can be corrected to less than 0.5 m when β^* is 0.75 and 1.00 m, but $D_y^{\max}$ exceeds 1 m after the correction when β^* is 0.5 m. The dispersion correction

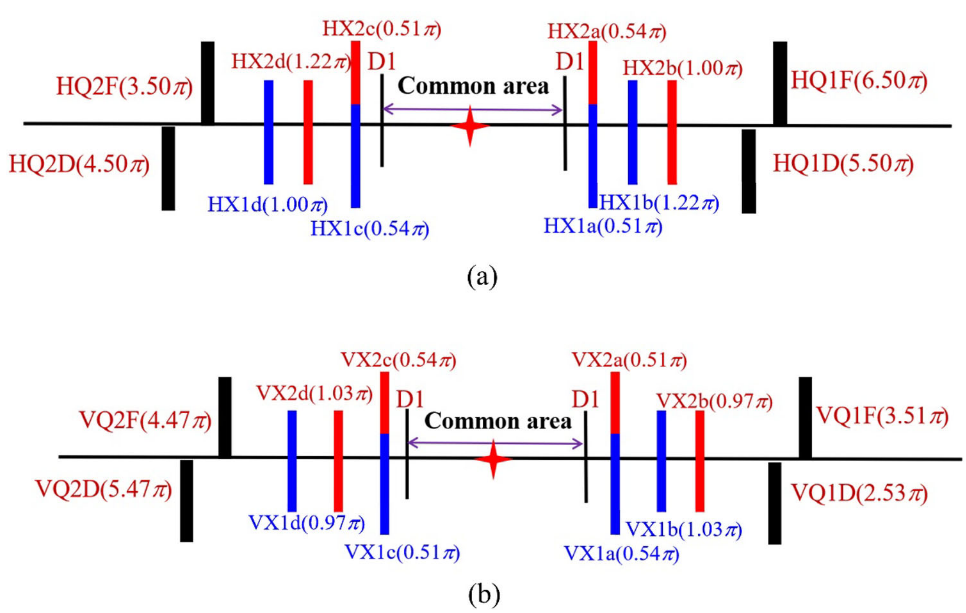

Fig. 3 (Color online) Sketch of dipole and quadrupole correctors in IR3 with horizontal crossing (**a**) and in IR7 with vertical crossing (**b**). D1 is the first separation dipole and the star symbols show the interaction points (IPs). The blue and red rectangles indicate dipole correctors for Beam 1 and Beam 2, respectively. The overlapping rectangles show the correctors for both beams in different beam pipes. The numbers in brackets are the phase advances from the element to the IP in the horizontal plane (**a**) or in the vertical plane (**b**). (HX, VX) are the dipole correctors generating crossing angles in IR3 and IR7, respectively**.** (HQ, VQ) are the quadrupole correctors in IR3 and IR7, respectively. (F, D) represents (focusing, defocusing) quadrupoles, respectively

Table 2 Dispersion values before and after adding quadrupole correctors at nominal parameters

Dispersion (D_x, D_y)	Without crossing	With crossing but no correctors	With crossing and correctors
(D_x, D_y) at IP3 (m)	(0, 0)	(0.002, 0)	(0, − 0.001)
(D_x, D_y) at IP7 (m)	(0, 0)	(0, − 0.002)	(0, 0)
Max (D_x, D_y) in IR3 (m)	(0, 0)	(1.38, 2.43)	(0.03, 0.01)
Max (D_x, D_y) in IR7 (m)	(0, 0)	(2.48, 1.28)	(0.01, 0.04)
Max (D_x, D_y) in ring (m)	(2.8, 0.0)	(2.91, 2.43)	(2.81, 0.29)

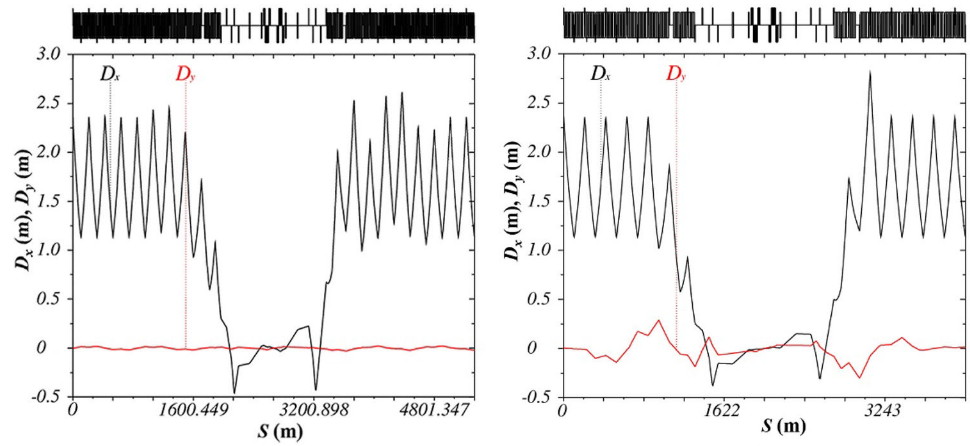

Fig. 4 Dispersion in two IRs and its neighboring arc regions with quadrupole correctors in IR3 (**a**) and IR7 (**b**). β^* is 0.75 m and crossing angle is 110 μrad at both IPs

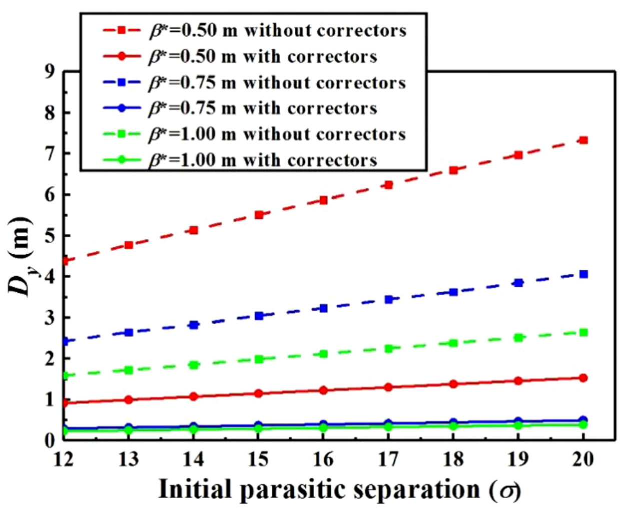

Fig. 5 (Color online) Maximum vertical dispersion D_y^{max} around the ring as a function of the initial parasitic separations with (solid) and without (dashed) quadrupole correctors

worsens with a smaller β^* and larger separation. Table 3 lists some key parameters for an initial parasitic separation of 20σ. It was assumed that the luminosity reduction was recovered with the use of crab cavities. When β^* is 0.5 m, the smallest physical aperture in the inner triplet drops to an unacceptably low value of 9σ and the beta-beating is intolerably large. This study indicates that large separations require a β^* greater than 0.5 m.

3.2 Beam–beam effects with constant emittance

3.2.1 Tune footprint and frequency map analysis

In the SPPC, the nominal tunes were (120.31, 117.32), and the fractional parts were the same as that in the LHC. The B–B parameter was 0.0075 for each IP. The tune footprints of a nominal bunch from both the theory mentioned in Sect. 2.2 and the simulations with all the B–B interactions for two different initial tunes are shown in Fig. 6 (previously used in a review article [29]). In the simulations, the tune footprint was obtained by tracking the particles with amplitudes ranging from 0 to 10$\sigma_{x,y}$ for 2048 turns. Chromaticity correction and momentum deviation were not included to consider the tune spread from only B–B interactions. All the sum and difference resonances up to the fourth order are shown. In both plots, the theoretical calculation predicts the main part of the tune footprint quite well, particularly in the area far from the resonances that are not included in the theory. Both plots show the effects of the difference coupling resonance driven by the skewed quadrupole components of the LRI. The figure on the left shows that a few particles are captured by the third-order

Table 3 Factors limiting the choice of β^* with initial separation of 20σ in all cases

	$\beta^* = 0.5$ m	$\beta^* = 0.75$ m	$\beta^* = 1$ m
Crossing angle (μrad)	221	184	160
Luminosity reduction factor due to crossing angle	0.55	0.69	0.79
Max β (m)	28,000	18,660	13,999
Smallest physical aperture (σ)	9	14	17
Beta-beating	16%	11%	9%
Linear chromaticity (before correction)	(− 313, − 312)	(− 259, − 258)	(− 232, − 231)

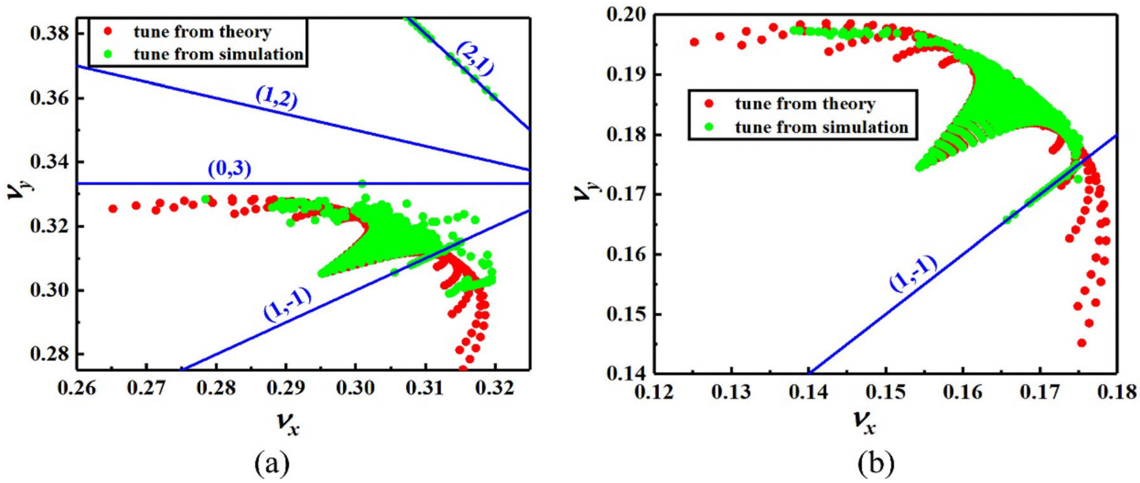

Fig. 6 (Color online) Footprint caused by beam–beam (B–B) interactions for different initial nominal tunes: **a** (0.31, 0.32) and **b** (0.17, 0.19). The red and green points represent the theoretical calculation and simulations, respectively. The lines show all the nearby resonances, up to the fourth order. The numbers (m, n) in brackets define the resonances $m\nu_x + n\nu_y = p$, where p is an integer

resonance $2\nu_x + \nu_y = 1$, which is also driven by the LRI. In the plot on the right, the harmful low-order sum resonances are far away, and there is no evidence of particle trapping.

To determine the contribution of different nonlinear kicks, Fig. 7 presents FMA plots for three cases comparing the effects of the HOIs and LRIs. The FMA plots were obtained by tracking the particles for 4096 turns. The amplitudes extend to a physical aperture of 23σ in the first plot compared to 10σ in the other two plots. This clearly shows that the tune diffusion increases significantly with the LRI compared to the HOI. The tune variation of particles with amplitudes between 6σ and 10σ increases by more than four orders of magnitude in the last two plots, which indicates that the LRI is the main source of particle instability. This conclusion is the same as that for LHC-like configurations, as expected [3, 13–14]. Although the LRI mainly impacts particles at large amplitudes, small-amplitude particles are also affected.

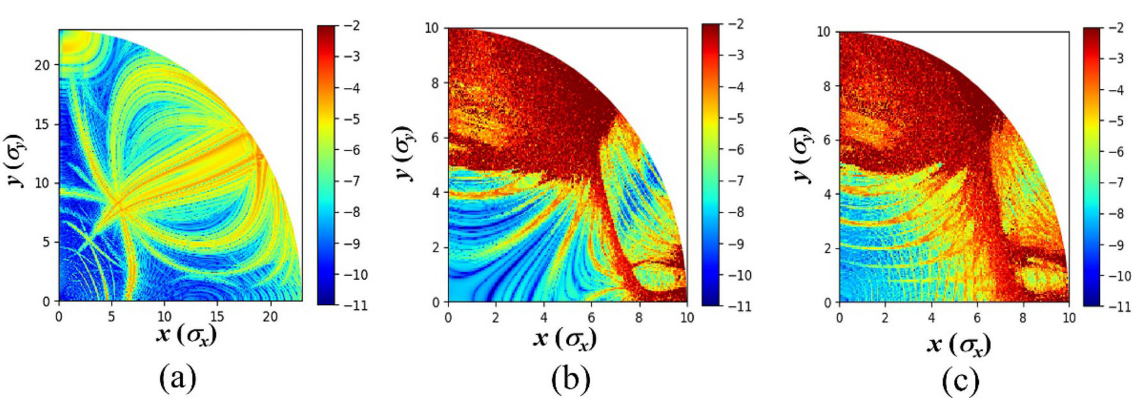

Fig. 7 (Color online) Frequency map analysis (FMA) plots with different B–B interactions: **a** Head-on interaction (HOI); **b** Long-range interaction (LRI); **c** HOI + LRI. Sextupole kicks are included in all cases

3.2.2 Dynamic aperture with nominal tunes

Particle instability based on FMA calculations must be checked using longer-term tracking. Thus, the DA was calculated by tracking the particles over 10^6 turns. The initial longitudinal distribution in z is Gaussian-truncated to $2\sigma_z$ and has a uniform momentum spread of $1\sigma_p$. The chromaticity was corrected to + 1 in both planes. The average DA was obtained by averaging over 15 azimuthal angles.

Four nonlinear cases are studied. The average DA values for both the nominal and Pacman bunches are listed in Table 4. Pacman bunches denote those bunches with fewer LRI in an IR because of the time gap between the bunch trains. In Table 4, the Pacman bunch has 41 LRIs in each IR, which is the least number of LRIs among all such bunches. The physical aperture (23σ) is taken as the average DA when the simulated average DA exceeds the physical aperture. We found that the DA for the nominal bunch is larger than the physical aperture without the LRI. These interactions reduce the DA to approximately 6σ. The HOI has a relatively small impact on the DA. Therefore, this demonstrates again that the LRI is the main source of particle loss among the included interactions. The same conclusion is true for the Pacman bunches. Figure 8 shows the distribution of the LRI separations in IR3. The first 12 LRIs before the first quadrupole occurred at a constant separation of 12σ. The minimum separation was 9σ–10σ. There are also six LRIs with a constant separation of 17σ on the right-hand side. Figure 9 shows the DA for different numbers of LRIs with different separations.

3.2.3 Dynamic aperture with tune scan

To operate accelerators effectively, the working points must be carefully selected; otherwise, the beam may be sensitive to errors and easily lost. Initially, the fractional tunes of the SPPC are the same as those in the LHC design, but a tune scan is performed to find better working points [30]. The DA is calculated with different fractional tunes, and the integer part remains unchanged. In the tune space, the resonance-free spaces are wider along the diagonal;

Table 4 Average dynamic aperture (DA) for four different cases. The physical aperture is 23σ

	DA-nominal (σ)	DA-Pacman (σ)
Sextupole	23	23
Sextupole + HOI	23	23
Sextupole + LRI	6.2	9.8
Sextupole + HOI + LRI	5.5	7.8

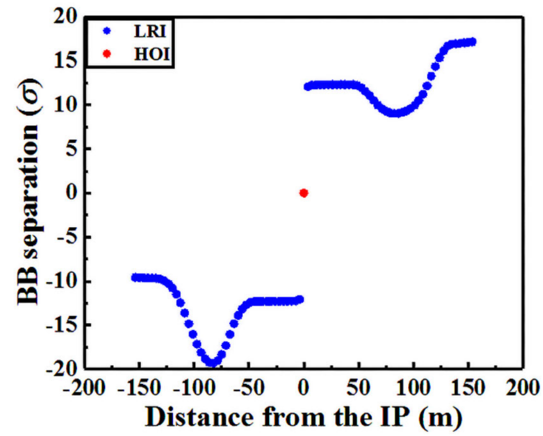

Fig. 8 (Color online) B–B separations in IR3 are normalized by their horizontal beam sizes. The blue dots denote the separations of LRIs and the red dot represents the HOI at the IP

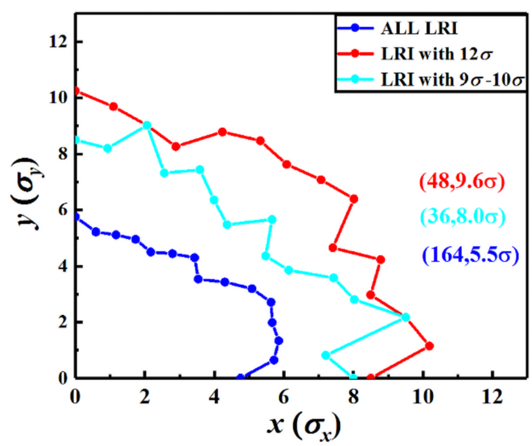

Fig. 9 (Color online) DA in amplitude space for different numbers of LRIs. The HOIs are included in all settings. The numbers in brackets show the number of LRIs and average DA. The blue/red/cyan lines show the average DAs with all LRIs, 48 LRIs at separations of 12σ, and LRIs at separations of (9–10)σ

thus, the initial tunes are scanned along the diagonal from (0.10, 0.10) to (0.46, 0.46) with a step size of 0.01. The tunes are split by keeping $|\nu_x - \nu_y|$ constant to avoid the strong influence of difference resonance. The tune separations are set to the values of (± 0.01, ± 0.02) to study the coupling effects due to the LRI. LHC studies also revealed that a better DA was observed with tunes close to the diagonal [31].

For a tune separation of 0.01, Fig. 10 shows the average DA versus the horizontal fractional tune, with and without a nominal crossing angle of 110 μrad. Independent of the crossing angle and momentum deviation, the DA declines rapidly when the fractional tunes approach the lower-order resonances in the fifth order (0.2), fourth order (0.25), and third order (0.33), while the drop at 0.4 only appears in the case with a crossing angle. Both the crossing angle and

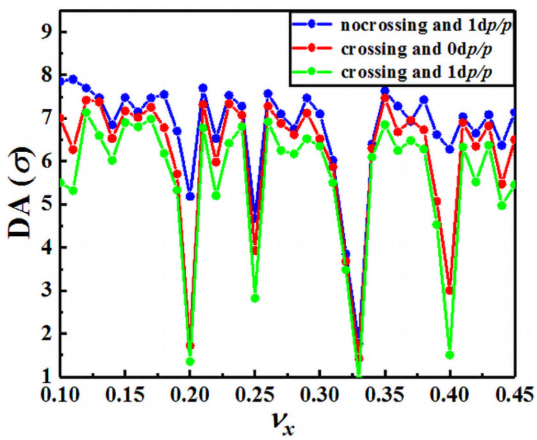

Fig. 10 (Color online) Average DA versus different horizontal tunes ($v_y = v_x + 0.01$). Blue: without a crossing angle and d$p/p = \sigma_p$; Red: with a crossing angle and no momentum deviation; Green: with a crossing angle and d$p/p = \sigma_p$

momentum spread cause some reduction in DA. The synchro-betatron resonances driven by the crossing angle are believed to cause this reduction [32].

A larger tune separation of 0.02 is also tested. The third-order resonances still reduce the DA but the fourth- and fifth-order resonances do not affect it. This implies that the tune separation of $|v_x—v_y| > 0.01$ seems to be safer. Table 5 summarizes the DA with the six best-found tunes and nominal tune. We find that the smallest DA is always approximately 1σ less than the average DA. Figure 11 shows the FMA plots in both the amplitude and frequency spaces for the nominal and two best tunes. We observe from the amplitude space plots that the tune diffusion is smaller at the best tunes for particle amplitudes ranging from 6 to 8σ. The plots in the tune space show that the footprint for the nominal tune is crossed by the third-order resonances, and the footprints for the other two tunes are crossed by fourth- and sixth-order sum resonances. As expected, the lower the order of the resonance, the smaller is the dynamic aperture. The tunes identified here could serve as good initial candidates for further detailed studies.

Table 5 DA for the six best tunes and nominal tune

Tunes	Average DA (σ)	Smallest DA (σ)
(0.12, 0.13)	7.13	6.25
(0.17, 0.19)	7.12	6.25
(0.27, 0.26)	7.02	6.00
(0.37, 0.35)	6.70	5.75
(0.19, 0.17)	6.57	5.75
(0.38, 0.37)	6.50	6.25
(0.31, 0.32)	5.50	4.75

3.3 Mitigation of the beam–beam effects

3.3.1 Long-range interactions with different parasitic separations

In the baseline design, the B–B transverse separation was set to 12σ at the first parasitic interaction with a full crossing angle of 110 µrad and β^* of 0.75 m. As discussed in Sect. 2.3, the LRI can be mitigated by increasing the parasitic separation. The separation at the first parasitic interaction was increased from 12σ to 20σ by adjusting the crossing angle and β^*. The separations at the other LRIs increase simultaneously, but not necessarily by the same amount. As stated in Sect. 3.1, $\beta^* = 0.5$ m and 1.0 m are also considered, and the same settings as those in Sect. 3.2.2 are used for the chromaticity correction and momentum spread.

Figure 12 shows the average DA versus the separation at the first parasitic interaction for the three values of β^*. As expected, increasing the separation is useful for the average DA, which is almost independent of β^* because the crossing angle is increased by scaling as $1/\sqrt{\beta^*}$. However, increasing the crossing angle causes luminosity loss, although the crab cavities can recover the loss; however, other negative effects still exist, as discussed in Sect. 2.3. Thus, active LRC is considered to improve beam stability or even allow operation at smaller crossing angles.

3.3.2 Compensation of long-range interactions

Figure 13 shows the ratio β_x/β_y at different parasitic interaction locations in IR3 at nominal $\beta^* = 0.75$ m. The ratio β_x/β_y is not constant, but varies from 0.2 to 4.6. Figure 14 shows the locations for installing the current wires for long-range compensation and e-lens for head-on compensation in IR3. The phase advances from the IP to the locations of the LRI are all close to π/2 in the two transverse phase planes. As mentioned in Sect. 2.4, it is impossible to fully compensate for the LRI with the current wires. The ideal location is approximately 497 m away from the IP with a ratio $\beta_x/\beta_y = 1$, and the phase advance between the IP and the wire is approximately 3π/2 in both planes. There are four current wires in total, with one wire on each side of the IP. Each wire is responsible for compensating for 41 LRIs on its side in the IR. The phase advance between the wire and the LRI is nearly π in both planes, and the transverse separation from the weak beam at the wire is 12σ. According to Eq. (13), the current for a wire 2.5 m long is 118.1 A. The tune footprint after LRC is shown in Fig. 15. As expected, the tune footprint becomes much smaller with the use of wires and is close to that with only the HOI.

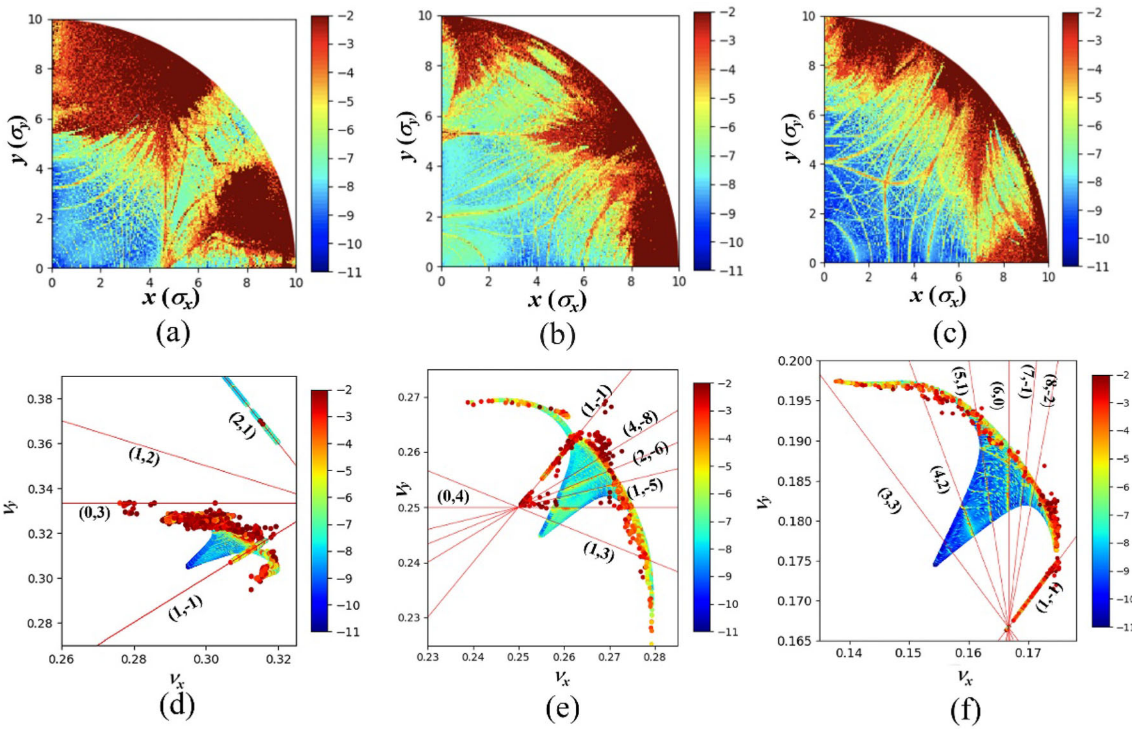

Fig. 11 (Color online) FMA plots in the amplitude (top) and frequency (bottom) spaces for the nominal tune (**a**, **d**), (0.27, 0.26) tune (**b**, **e**), and (0.17, 0.19) tune (**c**, **f**). The numbers (m, n) in brackets define the resonances $m\nu_x + n\nu_y = p$, where p is an integer

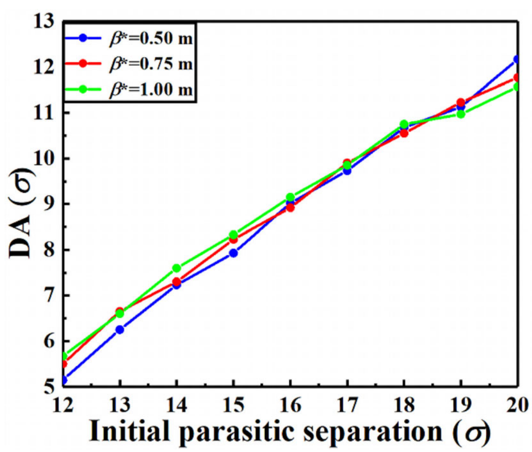

Fig. 12 (Color online) Average DA versus initial parasitic separation for different $\beta*$ values

Although the tune spread shrinks using wires, the resonance strength is more important for beam stability. Thus, DA simulations were performed to verify the effectiveness of compensation. The simulations for the HL-LHC found that the wires positioned at $\beta_x/\beta_y = 0.5$ or 2 were the most favorable, because the resonance driving term was found to be minimum [33]. Similar simulations of the DA were carried out for the SPPC, but the results showed that the compensation at $\beta_x/\beta_y = 1$ was still the best [34].

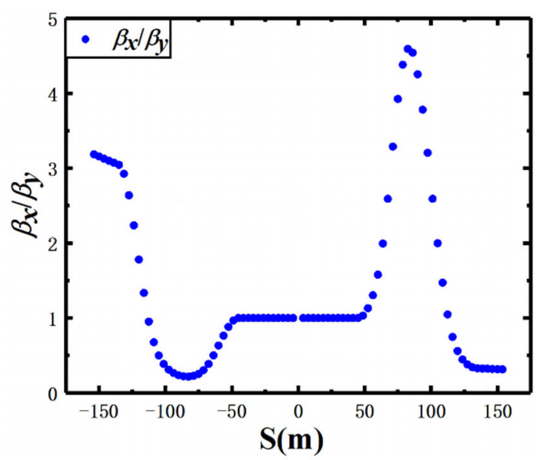

Fig. 13 Ratio β_x/β_y at all parasitic interaction locations in IR3

3.3.3 Compensation of head-on interactions

Although the above study shows that the LRI is dominant in determining the DA, the large tune spread caused by the HOI will have greater importance when all nonlinear components in the ring are included. Head-on compensation is considered an option, or even necessary, for future hadron colliders. In this subsection, the results of the compensation with an e-lens are presented.

Considering the conditions defined in Sect. 2.5, the electron beam was assumed to have a Gaussian

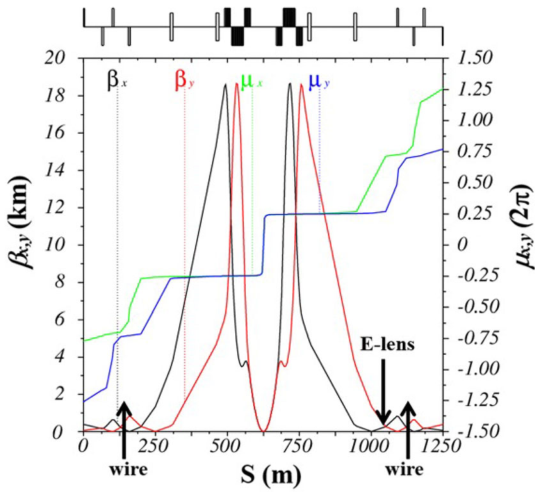

Fig. 14 (Color online) Phase advance and beta functions in IR3. The locations with $\beta_x/\beta_y = 1$ for the current wires and e-lens are marked with arrows

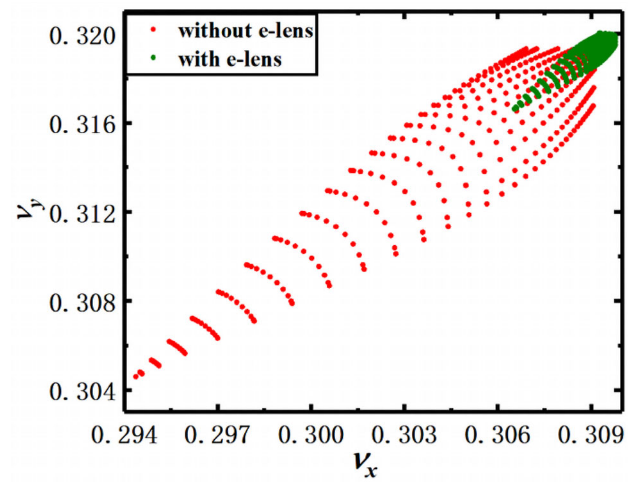

Fig. 16 (Color online) Tune footprints with amplitude from 0 to $8\sigma_{x,y}$ with (green) and without (red) HOC

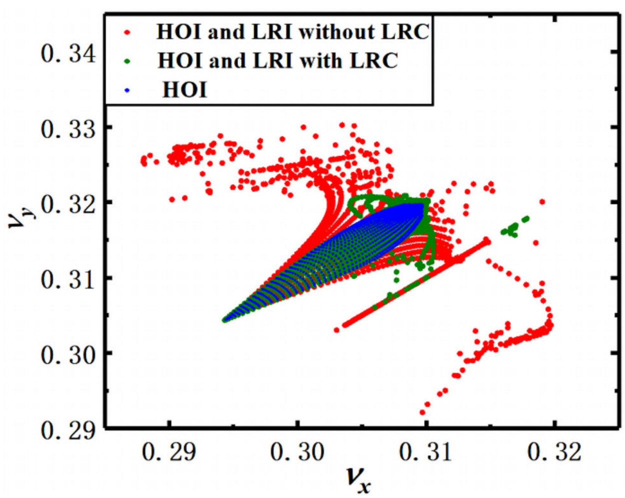

Fig. 15 (Color online) Tune footprints with amplitude from 0 to $15\sigma_{x,y}$ including all the interactions with and without LRC, and tune footprint including only HOI

distribution, similar to a strong beam. The kinetic energy of electrons is 10.53 keV, corresponding to a β_e of 0.2. With Eq. (14), N_e was calculated to be 1.25×10^{11}. Two e-lenses were distributed along the SPPC ring, one for each IR, as shown in Fig. 14. The e-lenses are located at the location with the same horizontal and vertical β but the phase advances between the e-lens and the IP are (1.42π, 0.54π) instead of the odd multiples of π. The effective length of the e-lens is 2 m.

Figures 16 and 17 show the tune footprints and tune diffusion with and without HOC. The tune spread was dramatically reduced with the compensation, but the tune diffusion rate increased at all particle amplitudes. Thus, we find that the HOC does not necessarily improve beam stability.

4 Beam–beam effects with emittance damping and particle burn-off

In the SPPC, emittance damping during a physics run increases the strength of the HOI and decreases the strength of the LRI as the relative separations increase. In general, a smaller emittance leads to higher luminosity. Thus, in this section, a detailed study to address the impact of B–B interactions with shrinking emittance is simulated. In addition, beam loss from collisions at the IPs was included.

4.1 Beam–beam effects with different emittances

This subsection presents studies on the effects of both HOIs and LRIs with varying emittance values. The simulations were carried out with different normalized emittances ranging from 2.4 μm (nominal value) to 0.2 μm, and the natural damping is estimated to require 6 h. The emittance damping is given by Eq. (12). The emittance values in the simulations were far greater than the calculated equilibrium emittance of 0.02 μm. Other parameters, such as the bunch intensity, were unchanged in these simulations. The results with a crossing angle of 110 μrad and longitudinal motion are shown in Fig. 18. The physical aperture and DA values in this figure were scaled by the RMS beam size at the normalized emittance to show the relative beam stability.

Figure 18a shows that as the emittance decreases from 2.4 to 0.2 μm, the physical aperture normalized by RMS beam size and B–B parameter increase as expected. The

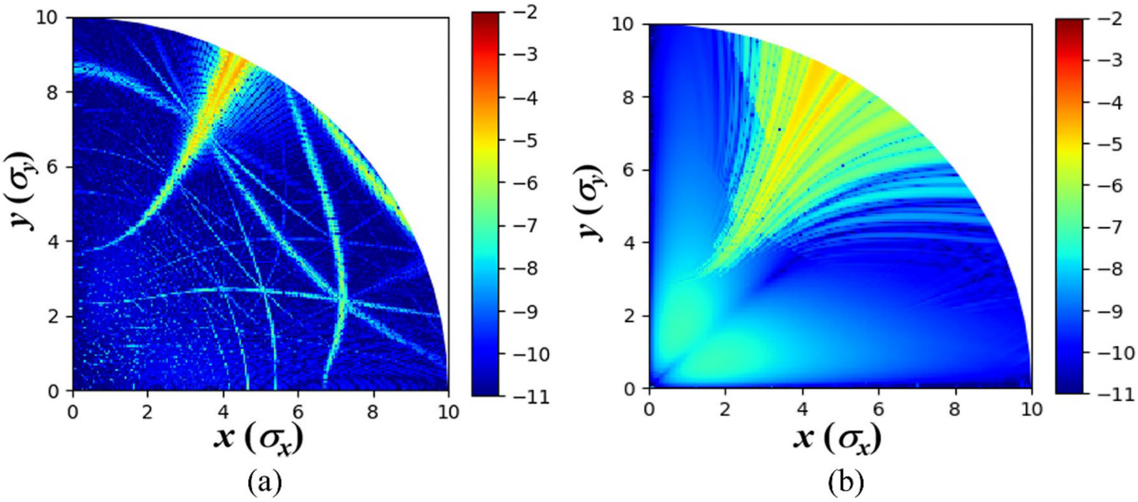

Fig. 17 (Color online) FMA plots in the amplitude space without (a) and with (b) HOC

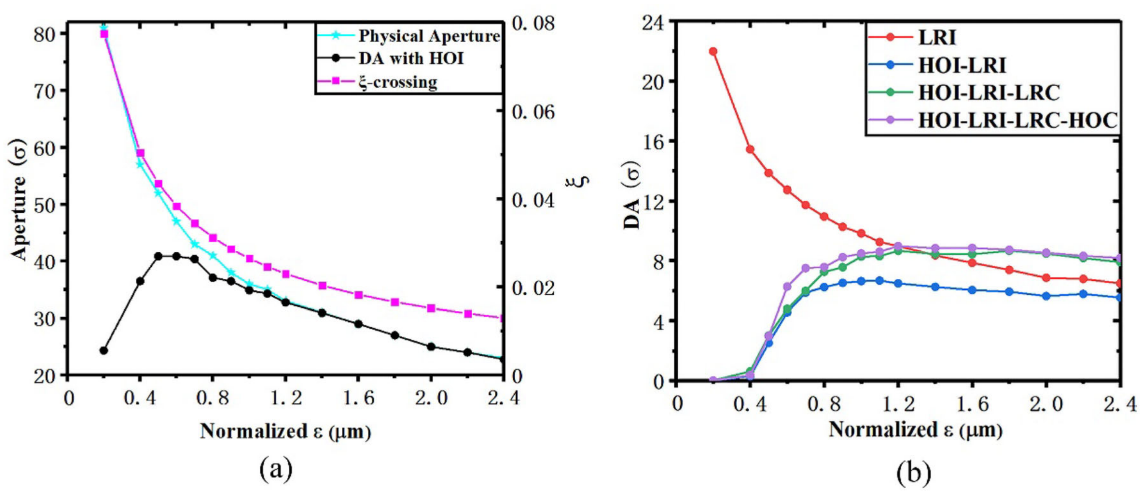

Fig. 18 (Color online) **a** Average DA and B–B parameter versus emittance with a crossing angle of 110 μrad and longitudinal motion (HOI alone); **b** average DA versus emittance with different B–B effects and correction schemes (LRI alone, HOI-LRI, HOI-LRI-LRC, HOI-LRI-LRC-HOC)

HOI alone does not cause beam loss at the initial stages of shrinking emittance but from 1.2 μm downward, the relative DA decreases. This verifies that the HOI gradually becomes considerably more important as the emittance decreases. As expected, the DA with the LRI alone improves with a smaller emittance, as shown in Fig. 18b. With combined HOI and LRI, the beam quality is dominated by the LRI from 2.4 μm to 1.2 μm and long-range compensation is effective in increasing the DA. However, the HOI dominates at smaller emittances, and both the LRC and HOC gradually lose their effectiveness. Thus, to maintain beam stability, for example, with a relative DA larger than 8σ, it will be necessary to slow down the fall in emittance by an emittance heating mechanism.

4.2 Beam–beam effects with emittance damping and particle burn-off

In addition to emittance damping, beam loss from luminosity also reduces the strength of the B–B interactions. Thus, we now consider both emittance shrinkage and beam loss in the DA simulations. The emittance evolution is assumed to follow Eq. (12). The loss rate of the bunch population owing to beam collisions follows from

$$\frac{\mathrm{d}N_{\mathrm{b}}}{\mathrm{d}t} = -\sigma_{\mathrm{tot}} n_{\mathrm{IP}} \frac{L}{n_{\mathrm{b}}}, \tag{16}$$

where n_{IP} is the number of interaction points; n_{b} is the number of bunches; and σ_{tot} is the total p–p cross section. Then, the bunch population evolution can be calculated by the following expression, which is derived by combining Eqs. (1), (12), and (16):

$$N_{\mathrm{b}}(t)=\frac{1}{\frac{1}{N_{\mathrm{b}}(0)}-\frac{2K\tau(He^{t/\tau}+1)^{1/2}}{He^{t/\tau}\varepsilon(0)}+\frac{2K\tau(He^{2t/\tau}+1)^{1/2}}{He^{t/\tau}\varepsilon(0)}},\tag{17}$$

$$K=\frac{\sigma_{\mathrm{tot}}fn_{\mathrm{IP}}}{4\pi\beta^*},\ H=\frac{(\sigma_z)^2\phi^2}{4\varepsilon(0)\beta^*},$$

where $N_{\mathrm{b}}(0)$ and $\varepsilon(0)$ are the initial bunch population and emittance, respectively. The constant K is related to the ideal luminosity, and H is related to the luminosity reduction factor owing to the crossing angle. The remaining parameters are defined in Sect. 2. With a zero-crossing angle, the bunch population evolution is [35]

$$N_{\mathrm{b}}(t)=\frac{1}{\frac{1}{N_{\mathrm{b}}(0)}-\frac{K\tau}{\varepsilon(0)}+\frac{K\tau e^{t/\tau}}{\varepsilon(0)}}.\tag{18}$$

The emittance and bunch population evolutions obtained using Eqs. (12) and (17) at a few discrete moments are shown in Fig. 19. The DA simulations in this section were performed with the inclusion of the crossing angle and synchro-betatron motion; all other conditions remained unchanged. In addition, a simulation with a zero-crossing angle for the HOI or without longitudinal motion was also carried out to understand the role of synchro-betatron coupling.

The simulation results are presented in Fig. 20 (previously used in a review article [29]). The B–B parameter increases monotonically with time. The DA with the combined HOI and LRI increases at first and starts decreasing at approximately 3 h. After compensating for the LRI, the DA improves by at least 2σ in the first 2 h and gradually declines until approximately 4 h when the LRC is no longer effective. This demonstrates that LRI is still

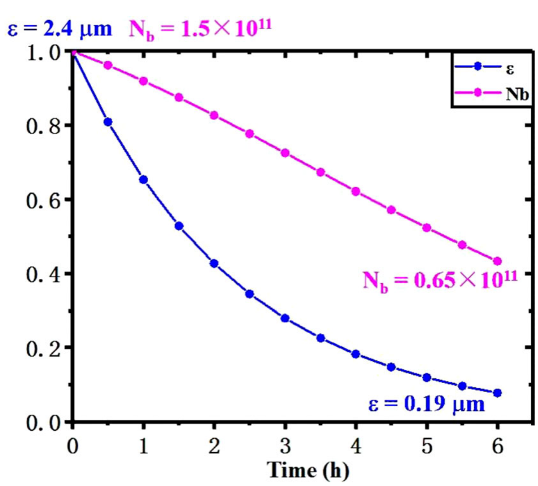

Fig. 19 (Color online) Evolutions of emittance and bunch population at different times. The initial and final values are marked

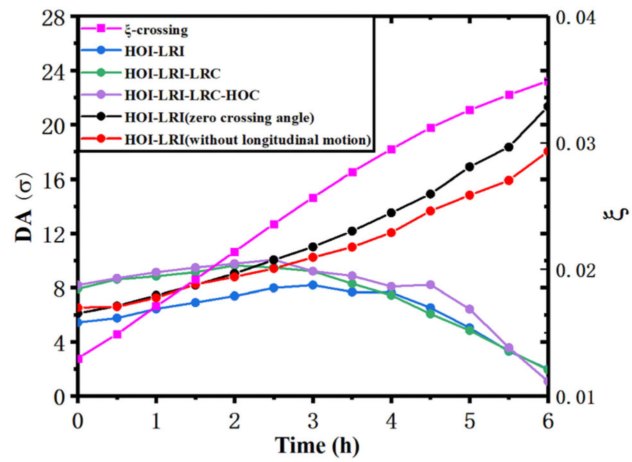

Fig. 20 (Color online) Evolutions of the average DA (circles) and B–B parameter (squares) with time including particle burn-off

the main limitation of beam stability in the initial stages, and HOI together with synchro-betatron coupling becomes more important in the later stages.

When the HOI and LRI are both compensated, the DA is nearly the same as that with LRC alone in the first 4 h, but HOC increases the DA from 4 to 5.5 h, as shown in Fig. 20. This demonstrates that HOC is effective when the HOI is dominant. The simulations also show that after 5.5 h, both HOC and LRC have no beneficial effects in improving the DA, but the DA without longitudinal motion or with zero-crossing angle still increases in this period. This can be explained by the synchro-betatron coupling at a smaller emittance, which is the driving mechanism of DA reduction. As mentioned in Sect. 2.3, crab cavities at IPs can be used to suppress the synchro-betatron coupling.

The DA in the LHC [36] and HL-LHC [14] must be at least 6σ. The simulations for HL-LHC found that the multipole magnetic field errors did not have a significant impact on the beam dynamics in the case of strong B–B interactions [14]. In the SPPC, the average DA goal is set to 8σ, considering that the smallest DA is approximately 1σ smaller than the average DA, and the contribution of high-order magnetic field errors is not included. However, as shown in Fig. 20, the average DA is below 8σ after 4.5 h, even with both HOC and LRC. To restore the beam stability without using an emittance heating mechanism that sacrifices luminosity, a DA goal of 8σ can be achieved by jointly applying crab cavities and LRC.

In the SPPC, luminosity optimization and leveling have been studied for different possible operation scenarios by considering limitations, such as those from the B–B parameter and event pileup per crossing [37]. When the B–B parameter sets the limit of luminosity optimization in the SPPC, a comparatively realistic operation scheme is shown in Fig. 21. The evolutions of some important parameters

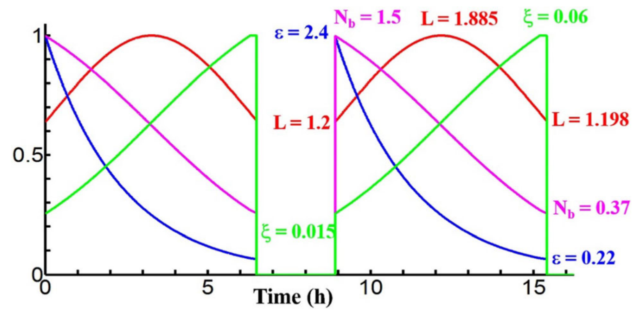

Fig. 21 (Color online) Evolution of the collision parameters over two cycles. The red, blue, magenta, and green colors denote the luminosity (in 10^{35} cm^{-2} s^{-1}), emittance (in μm), bunch population (in 10^{11}), and B–B parameter

(luminosity for each IP, bunch population, emittance, and B–B parameter for two IPs) with the run time in two cycles are presented. We assume that with crab cavities and LRC present, the DA is no longer the limiting factor; thus, the emittance is naturally damped before reaching the B–B parameter limit of 0.06 with two IPs when a new collision cycle is started. A peak luminosity of 1.885×10^{35} cm^{-2} s^{-1} occurs in the middle of a physics run. Finally, for each IP, an optimum average luminosity of 1.19×10^{35} cm^{-2} s^{-1} and annual integrated luminosity of 1.15 ab^{-1} are obtained, assuming an operation time of 160 days and a machine availability of 70%. Accordingly, if the maximum B–B parameter should be set to a lower value (e.g., 0.03 with two IPs), emittance heating must be applied earlier and the integrated luminosity will be lower.

5 Conclusion

In this study, the B–B effects as the main limit of luminosity optimization in the SPPC are investigated, including two major parts: one with a constant emittance, and the other considering the transverse emittance shrinking due to synchrotron radiation and particle burn-off during collision.

With a constant emittance, the beam properties, including the tune footprint, FMA plots, and DA, are studied. The LRI is demonstrated to be the main factor limiting the particle stability, and the LRI effect on the DA is directly related to the LRI separations. Tune scan analysis is performed to find better tunes, and the third-, fourth-, and fifth-order resonances are found to be driven by the B–B interactions. A useful option to increase the DA significantly is to increase the crossing angle and adjust β^* together to increase the LRI separations, with a sacrifice in luminosity. The study of head-on and long-range compensations demonstrates that the tune footprint can be reduced with HOC or LRC, but only LRC improves the DA effectively.

The shrinking of the transverse emittance can mitigate the LRI, but conversely strengthen the HOI. The LRC is effective at restoring the DA before the emittance decreases to below a certain value, e.g., 0.7 μm, in the simulations. The HOC does not directly contribute to increasing the DA at the earlier stages of shrinking emittance, but it is modestly helpful when the emittance becomes small (e.g., 0.6 μm and 0.7 μm) in the simulations. However, for a very small emittance, synchro-betatron coupling becomes dominant in limiting the DA and can be compensated only with crab cavities. Finally, the luminosity optimization is studied with both emittance shrinking and particle burn-off. Crab cavities and LRC are assumed to guarantee an average DA goal of 8σ. With an assumed B–B parameter limit of 0.06 for two IPs, the average luminosity for each IP can be optimized to be 1.2×10^{35} cm^{-2} s^{-1}, which is sufficient to meet the SPPC design goal.

We note that these studies do not include several effects, such as coherent B–B effects, high-order field components in the IR magnets, nonlinear IR chromaticity correction, alignment, and gradient errors. Further studies are required for a detailed assessment.

Acknowledgements We would like to thank all the colleagues in the SPPC collaboration. We especially thank Prof. Philippe Piot and Northern Illinois University for their hospitality in hosting the visit of the first author, L. W., and the China Scholarship Council for supporting her to study at NIU and Fermilab.

Author contributions All authors contributed to the study conception and design. Material preparation, data collection, and analysis were performed by Li-Jiao Wang, Tanaji Sen, Jing-Yu Tang, and Lin-Hao Zhang. The first draft of the manuscript was written by Li-Jiao Wang and all authors commented on previous versions of the manuscript. All authors read and approved the final manuscript.

References

1. L.R. Evans, J. Gareyte, Beam-beam and single beam effects in the SPS proton-antiproton collider. IEEE T. Nucl. Sci. **30**, 2397–2399 (1983). https://doi.org/10.1109/TNS.1983.4332826
2. M. Harrison, R. Schmidt, The performance of proton antiproton colliders, in *Proc. 2nd European Particle Accelerator Conference*, Nice, France, 55–59 (1990). https://inspirehep.net/files/0d541cfdd986e009a2147bee4505d9c6
3. Y. Papaphilippou, F. Zimmermann, Weak-strong beam-beam simulations for the Large Hadron Collider. Phys. Rev. ST Accel. Beams **2**, 104001 (1999). https://doi.org/10.1103/PhysRevSTAB.2.104001
4. T. Sen, B. Erdelyi, M. Xiao et al., Beam-beam effects at the Fermilab Tevatron: Theory. Phys. Rev. ST Accel. Beams **7**, 041001 (2004). https://doi.org/10.1103/PhysRevSTAB.7.041001
5. L.L. Zhu, B. Wang, M. Wang et al., Energy and centrality dependence of light nuclei production in relativistic heavy-ion collisions. Nucl. Sci. Tech. **33**, 45 (2022). https://doi.org/10.1007/s41365-022-01028-8

6. M. Wang, J.Q. Tao, H. Zheng et al., Number-of-constituent-quark scaling of elliptic flow: a quantitative study. Nucl. Sci. Tech. **33**, 37 (2022). https://doi.org/10.1007/s41365-022-01019-9
7. H. Wang, J.H. Chen, Anisotropy flows in Pb–Pb collisions at LHC energies from parton scatterings with heavy quark trigger. Nucl. Sci. Tech. **33**, 15 (2022). https://doi.org/10.1007/s41365-022-00999-y
8. J.Y. Tang, J.S. Berg, W.P. Chai et al., Concept for a future super proton-proton Collider. (2015). https://arxiv.org/abs/1507.03224
9. J.Q. Yang, Y. Zou, J.Y. Tang, Collimation method studies for next-generation hadron colliders. Phys. Rev. Accel. Beams **22**, 023002 (2019). https://doi.org/10.1103/PhysRevAccelBeams.22.023002
10. H.J. Kim, T. Sen, Beam-beam simulation code BBSIM for particle accelerators. Nucl. Instrum. Methods Phys. Res. A **642**, 25–35 (2011). https://doi.org/10.1016/j.nima.2011.03.059
11. Y. Papaphilippou, F. Zimmermann, Estimates of diffusion due to long-range beam-beam collisions. Phys. Rev. ST Accel. Beams **5**, 074001 (2002). https://doi.org/10.1103/PhysRevSTAB.5.074001
12. V. Shiltsev, Y. Alexahin, V. Lebedev et al., Beam-beam effects in the Tevatron. Phys. Rev. ST Accel. Beams **8**, 101001 (2005). https://doi.org/10.1103/PhysRevSTAB.8.101001
13. J. P. Koutchouk, G. Sterbini, F. Zimmermann, Long-range beam-beam compensation in the LHC. International Committee for Future Accelerators, ICFA, Beam Dynamics Newsletter No. 52, 81–95 (2010). http://cds.cern.ch/record/1289711
14. D. Banfi, J. Barranco Garcia, T. Pieloni, Dynamic aperture studies for HL-LHC with beam-beam effects. CERN-ACC-NOTE-2017-0035 (2017). http://cds.cern.ch/record/2263345?ln=zh_CN
15. Y. Nosochkov, D.M. Ritson, The provision of IP crossing angles for the SSC, in *Proc. Particle Accelerator Conference*, Washington, DC, USA, 125–127 (1993). https://inspirehep.net/files/54796c1b0cebbc83ef4676311be7f5eb
16. O. Brüning, W. Herr, R. Ostojic, A beam separation and collision scheme for IP1 and IP5 at the LHC for optics version 6.1. LHC Project Report 315 (1999). http://cds.cern.ch/record/407317?ln=zh_CN
17. F. M´eot, Crossing angle induced dispersion in LHC. FERMI-LAB-TM- 2001 (1997). https://lss.fnal.gov/archive/1997/tm/TM-2001.pdf
18. A. Piwinski, Limitation of the luminosity by satellite resonances. DESY 77/18 (1977). https://doi.org/10.3204/PUBDB-2017-12208
19. T. Sen, Crossing angle option for HERA. DESY-HERA-96–02 (1996). http://cds.cern.ch/record/299368?ln=zh_CN
20. F. Antoniou, Y. Papaphilippou, Analytical considerations for linear and nonlinear optimization of the theoretical minimum emittance cells: application to the compact linear collider predamping rings. Phys. Rev. ST Accel. Beams **17**, 064002 (2014). https://doi.org/10.1103/PhysRevSTAB.17.064002
21. A.W. Chao, Beam-beam instability, SLAC-PUB-3179 (1983). http://www.slac.stanford.edu/pubs/slacpubs/3000/slac-pub-3179.pdf
22. J.P. Koutchouk, Principle of a correction of the long-range beam-beam effects in LHC using electromagnetic lenses. LHC Project Note 223 (2000). http://cds.cern.ch/record/692058?ln=zh_CN
23. U. Dorda, Compensation of long-range beam-beam interaction at the CERN LHC. CERN-THESIS-2008-055 (2008). http://cds.cern.ch/record/1114782?ln=zh_CN
24. B. Erdelyi, T. Sen, Compensation of beam-beam effects in the Tevatron with wires. FERMILAB-TM-2268 (2004). https://inspirehep.net/literature/662654
25. E. Tsyganov, R. Meinke, W. Nexsen et al., Compensation of the beam-beam effect in proton-proton colliders. SSCL Report No.519 (1993). https://inspirehep.net/literature/359786
26. E. Tsyganov, A. Taratin, A. Zinchenko, Compensation of space charge effect at beam-beam interactions in proton-proton colliders. JINR-E9-96-4 (1996). https://inspirehep.net/literature/420296
27. Y. Luo, W. Fischer, N.P. Abreu et al., Six-dimensional weak-strong simulation of head-on beam-beam compensation in the Relativistic Heavy Ion Collider. Phys. Rev. ST Accel. Beams **15**, 051004 (2012). https://doi.org/10.1103/PhysRevSTAB.15.051004
28. V. Shiltsev, V. Danilov, D. Finley et al., Considerations on compensation of beam-beam effects in the Tevatron with electron beams. Phys. Rev. ST Accel. Beams **2**, 071001 (1999). https://doi.org/10.1103/PhysRevSTAB.2.071001
29. J.Y. Tang, Design concept for a future super proton-proton collider. Frontiers Phys. **10**, 828878 (2022). https://doi.org/10.3389/fphy.2022.828878
30. Z.X. Song, W.D. Deng, G. de Lentdecker et al., Study of the retina algorithm on FPGA for fast tracking. Nucl. Sci. Tech. **30**, 127 (2019). https://doi.org/10.1007/s41365-019-0643-x
31. D. Pellegrini, F. Antoniou, S. Fartoukh et al., Multiparametric response of the LHC Dynamic Aperture in presence of beam-beam effect, in *Proc. 8th International Particle Accelerator Conference*, Copenhagen, Denmark, 2051–2054 (2017). https://doi.org/10.1088/1742-6596/874/1/012006
32. A. Piwinski, Satellite resonances due to the beam-beam interaction. IEEE T. Nucl. Sci. **24**, 1408–1410 (1977). https://doi.org/10.1109/TNS.1977.4328960
33. S. Fartoukh, A. Valishev, Y. Papaphilippou et al., Compensation of the long-range beam-beam interactions as a path towards new configurations for the high luminosity LHC. Phys. Rev. ST Accel. Beams **18**, 121001 (2015). https://doi.org/10.1103/PhysRevSTAB.18.121001
34. L.J. Wang, T. Sen, Weak-strong simulation of beam-beam effects in super proton-proton collider, in *Proc. North American Particle Accelerator Conference*, Lansing, MI, USA, 22–25 (2019). https://doi.org/10.18429/JACoW-NAPAC2019-MOYBA5
35. M. Benedikt, D. Schulte, F. Zimmermann, Optimizing integrated luminosity of future hadron colliders. Phys. Rev. ST Accel. Beams **18**, 101002 (2015). https://doi.org/10.1103/PhysRevSTAB.18.101002
36. J.P. Koutchouk, for the LHC Team, The LHC Dynamic Aperture, in *Proc. Particle Accelerator Conference*, New York, 372–376 (1999). https://inspirehep.net/literature/499741
37. L.J. Wang, J.Y. Tang, Luminosity optimization and leveling in the super proton-proton collider. Radiat. Detect. Technol. Meth. **5**, 245–254 (2021). https://doi.org/10.1007/s41605-020-00233-6